

# A closer view of the IGR J11014-6103 outflows

L. Pavan<sup>1</sup>, G. Pühlhofer<sup>2</sup>, P. Bordas<sup>3</sup>, M. Audard<sup>1</sup>, M. Balbo<sup>1</sup>, E. Bozzo<sup>1</sup>, D. Eckert<sup>1</sup>, C. Ferrigno<sup>1</sup>, M. D. Filipović<sup>4</sup>,  
M. Verdugo<sup>5</sup>, and R. Walter<sup>1</sup>

<sup>1</sup> Université de Genève, Departement d’Astronomie – ISDC, chemin d’Ecogia, 16, 1290 Versoix, Switzerland  
e-mail: Lucia.Pavan@unige.ch

<sup>2</sup> Institut für Astronomie und Astrophysik, Universität Tübingen, Sand 1, D-72076, Tübingen, Germany

<sup>3</sup> Max-Planck-Institut für Kernphysik Saupfercheckweg 1, D-69117, Heidelberg, Germany

<sup>4</sup> Western Sydney University, Locked Bag 1797, Penrith South DC, NSW 1797, Australia

<sup>5</sup> Department for Astrophysics, University of Vienna Türkenschanzstr. 17, 1180 Vienna, Austria

Received / Accepted

## ABSTRACT

The complex X-ray system IGR J11014-6103 (a.k.a. the Lighthouse nebula) is composed of a bow-shock pulsar wind nebula (PWN) as well as large-scale jet-like features, all launched by IGR J11014-6103 which is moving supersonically in the interstellar medium. Previous observations suggested that the jet features stem from a ballistic jet of relativistic particles. In order to confirm the nature of the jet and the marginally detected counter-jet, we obtained a new deep 250 ks *Chandra* observation of the Lighthouse nebula. We performed detailed spatial and spectral analysis of all X-ray components of the system. The X-ray PWN is now better resolved and shows a clear bi-modal morphology. The overall helical pattern of the main jet is confirmed. However, there are large deviations from a simple helical model at small and large scales. Significant extended emission is now detected, encompassing the main jet all along its length. The brightness dip of the main jet at  $\sim 50''$  distance from the pulsar is confirmed, the extended emission however prevents conclusions about the coherence at this position of the jet. The counter-jet is now detected at high statistical significance. In addition, we found two small-scale “arcs” departing from the pulsar towards the jets. We also looked for possible bow-shock emission in front of the pulsar, with a short VLT/FORS2 H- $\alpha$  observation. No clear emission is found, most likely because of contamination from a diffuse surrounding nebulosity. The results of our X-ray analysis show that current expectations from a ballistic nature of the jets can explain satisfactorily some of the observational evidences but cannot fully reproduce the observations. The alternative scenario (diffusion of particles along preexisting magnetic field lines in the surrounding medium) however also continues to suffer from conflicts with the observations.

**Key words.** X-rays: individuals: IGR J11014-6103; supernovae: individual: MSH 11-61A; Stars: neutron; Stars: jets; ISM: jets and outflows; ISM: supernova remnants

## 1. Introduction

Neutron stars are one of the possible end points of the stellar evolution, and are produced in most cases through the degenerate collapse of the core of a massive star (once the internal part of the star has reached an unstable condition). This core-collapse supernova explosion can imprint a strong natal kick to the newly born neutron star, which can consequently move with high velocity into the ambient medium (see e.g. the review by Janka 2012). Detailed analyses of the galactic pulsar population found a mean velocity of  $\sim 400$  km/s (Hobbs et al. 2005). The highest velocity directly measured is that of PSR B1508+55 with  $v_{\text{PSR}} = 1083^{+103}_{-90}$  km/s (Chatterjee et al. 2005).

When the spatial velocity of a pulsar is sufficiently large, it will escape its progenitor’s supernova remnant (SNR) while the SNR is still young and active e.g. in X-rays. The pulsar’s motion in the interstellar medium ISM is then typically supersonic. In this case, a bow-shock is generated in front of the pulsar, and the swept-up matter prevents the wind expelled by the pulsar to propagate in the direction of motion. This wind is then collimated backwards, forming a nebula confined in a conical shape (whose aperture angle depends, among other parameters, on the pulsar linear velocity; for a review see, e.g. Gaensler 2005).

MSH 11-61A (a.k.a. G290.1-0.8) is a mixed morphology SNR detected from radio to soft X-rays (up to  $\sim 3$  keV), formed by the core collapse of a massive progenitor star (mass  $\gtrsim 25M_{\odot}$ ; Filipović et al. 2005; Reynoso et al. 2006; García et al. 2012; Kamitsukasa et al. 2015; Auchettl et al. 2015a). Following these authors, the distance to the SNR is in the range 6 -11 kpc, with the latest values converging towards  $7 \pm 1$  kpc. This distance of 7 kpc is adopted throughout the paper<sup>1</sup>. Close to this SNR is the INTEGRAL source IGR J11014-6103 – an X-ray system powered by the pulsar PSR J1101-6101 and comprising several extended structures (Pavan et al. 2011; Tomsick et al. 2012; Pavan et al. 2014, hereafter Paper II; Halpern et al. 2014). Previous *Chandra* observations that were aimed at the INTEGRAL source identified these structures as three outflows produced by PSR J1101-6101: an X-ray and radio PWN, shaped in a narrow cone elongated towards the parent SNR, and an X-ray jet and counter-jet, both oriented nearly perpendicular to the PWN axis (Tomsick et al. 2012, Paper II). The main jet extends for nearly  $5'$  in the sky, which corresponds to a length of  $\sim 11$  pc projected on the plane of the sky, at the 7 kpc distance, and showed a remarkable helicoidal pattern (see Paper II). Already in this data

<sup>1</sup> for reference, at the distance of 7 kpc an angular scale of 1 arcmin corresponds to  $\sim 2$  pc.

set, indications for a spatial deviation from the helical pattern of the main jet were present at  $\sim 50''$  distance from the pulsar. At this position the surface brightness of the jet is low (seemingly a “gap”), but the brightness profile was compatible with expectations due to Doppler-deboosting in the jet-helix model. The spatial deviation was therefore not considered significant at the time, also because the data were hampered by the presence of CCD chip gaps, resulting in only 50% effective exposure in that region. The spatial deviation was therefore not considered significant at the time.

The counterjet was detected at  $3.7\sigma$  in the *Chandra* image and characterised by a flux of  $\sim 5\%$  that of the main jet. The conical shape of the PWN in IGR J11014-6103 is ascribed to the supersonic motion of PSR J1101-6101 in the ISM (Tom-sick et al. 2012). Although several examples of bow-shock pulsar wind nebulae (bsPWNe) have now been detected in connection with their pulsars travelling at supersonic velocities in the interstellar medium (see e.g. Gaensler et al. 2004; McGowan et al. 2006; Kargaltsev & Pavlov 2008), only one other system is sharing a geometry similar to the one seen in the Lighthouse nebula: the Guitar nebula, powered by PSR B2224+65 (Cordes et al. 1993; Chatterjee & Cordes 2002; Johnson & Wang 2010; Hui et al. 2012). In this source the pulsar is powering a bright and elongated X-ray jet as well, extending over  $\sim 1$  pc in a direction almost perpendicular to pulsar direction of motion. In both cases, that of the Lighthouse nebula and that of the Guitar nebula, the mechanism leading to the production of such peculiar jets is still poorly understood (Bandiera 2008, Johnson & Wang 2010, Pavan et al. 2011, Hui et al. 2012, Paper II).

To solve a series of questions that could not be conclusively addressed with the previous data set, we obtained in 2014 a much deeper *Chandra* X-ray observation (250 ks), the analysis of which we describe here in Sect. 2. In contrast to our first *Chandra* observation that was aimed at imaging with the highest accuracy the pulsar and the PWN, we centered this second observation on the main jet to investigate its intriguing morphology. The observation was split into 5 smaller exposures (with different roll angles) because of planning constraints. We then chose to optimise the pointing displacement to have the main jet (and the pulsar) entirely included in a single (and same) CCD, in order to optimally investigate the “gap” region along the main jet, and the region connecting the pulsar and the jet base. This was achieved with a *simZ* offset of 6.0 mm and a *Y* offset of 1.0'. The offsets were kept identical in all exposures to ensure a good handling of the combined events. We report here also on the analysis of an exploratory observation performed with VLT to search for possible H- $\alpha$  emission close to the pulsar (Sect. 3). In Sect. 4 we discuss the results of our data analyses, and provide our conclusions in Sect. 5.

## 2. *Chandra* X-ray observations and data analysis

The new *Chandra* observation was split into 5 shorter exposures, as detailed in Table 1. The data have been processed with *Chandra* CIAO v.4.7, using the latest available calibrations (CALDB v. 4.6.7). All observations have been reprocessed with the CIAO tool *chandra\_repro*, using *vfaint* mode background cleaning and subpixel resolution (*edser* method), unless differently specified. After cleaning, we verified that this filter did not affect significantly the event counts of the emitting structures in IGR J11014-6103. Only the pulsar was partially affected by this filter, with  $\sim 6\%$  of good events being rejected. We used therefore the *vfaint* background cleaned *evt2* files in the following.

**Table 1.** Summary of the *Chandra* observations of IGR J11014-6103

Obs ID	Exposure (ks)	Roll Angle (deg)	Obs Date
<i>new observation</i>			
16007	116.0	189.2	2014-08-28
16517	52.0	181.5	2014-09-05
16518	10.0	155.2	2014-09-29
17422	49.4	155.2	2014-10-01
17421	19.8	155.2	2014-10-02
<i>previous obs</i>			
13787	49.4	142.3	2012-10-11

We also verified that the observations were not affected by high flaring background. The total cleaned exposure time was 247 ks.

By computing and inspecting the PSF map of each observation, we verified that in all cases the characteristics of the instrument PSF were virtually constant in the region including the pulsar, the jets, and the PWN.

### 2.1. Imaging

The new observations were combined in an exposure corrected mosaic with the *ciao* tool *merge\_obs*, in the energy range 0.5-7 keV (see Fig. 1). The main spatial features seen in this mosaic are:

**PWN:** The PWN has a sharp conical shape, but it also shows a more extended and collimated component. The overall structure resembles the shape of an arrow, with the “shaft” of the arrow extending over  $\sim 1.7'$  in a compact cylindrical shape, and the “head” extending on a wider and slightly dimmer cone, with an aperture of  $\sim 30^\circ$  up to  $\sim 0.7'$  from the pulsar (see inset in Fig. 1). Comparing the new image to our previous 50 ks observation, we note that the same structure was present also in that observation, but less evident because of the lower statistics.

**counter-jet:** The counter-jet is now very significantly detected and it extends remarkably linearly for  $1.5'$ , in SE direction. It also appears to be roughly aligned with the first  $50''$  of the main jet.

**Main jet:** Overall the main jet still shows the same pattern found in our previous shorter observation (Paper II), including a spatial “break” at about  $50-90''$  from the pulsar. Whereas in the previous observation this region was coincident with a factor two lower exposure due to the presence of ACIS chip gaps, the new data have equal exposure along the jet, without chip gaps or other significant dead chip columns. We can thus confirm that the loss of a coherent line structure is intrinsic to the emission from this region, and not due to instrumental artefacts. Lower surface-brightness emission is now also clearly detected, enshrouding the jet all along its length. Due to this emission, it is not possible to determine from the image whether the seeming “gap” is a true spatial break/decollimation of the jet, or whether the emission from the main jet is just dimming and mixed with the surrounding emission in this region (see also Sect. 2.3).

**Arcs:** In addition to the main spatial features described above, visual inspection of the mosaic image at small scales around the pulsar reveals the presence of an “arc” departing from the pulsar position towards the counter-jet (see inset in Fig. 1), with hints for the presence of a second, almost symmetric, arc west of the pulsar (i.e. towards the main jet). Because of the relatively low S/N level of the arc emission at larger distances

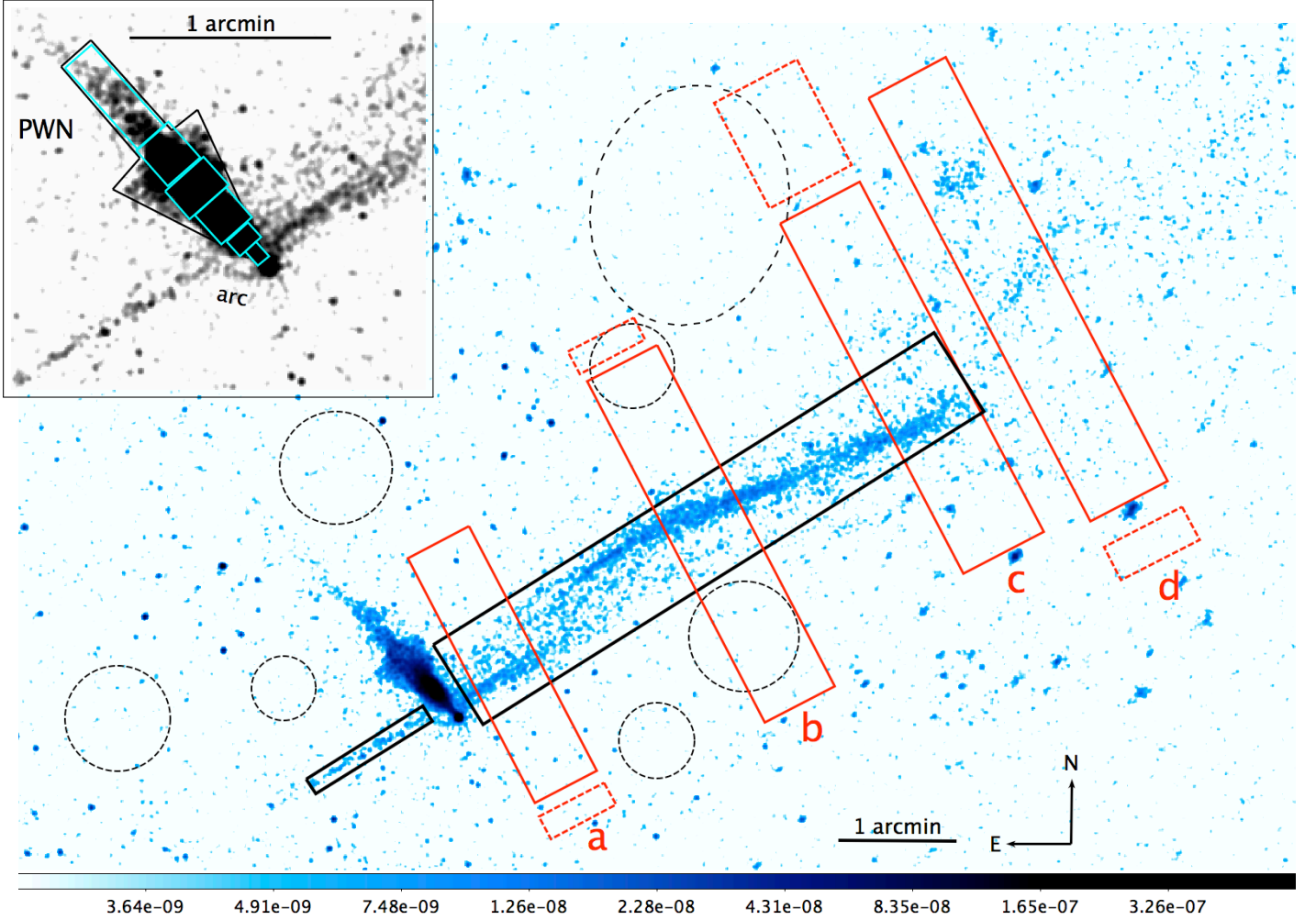


**Fig. 1.** *Chandra* 250 ks mosaic of the Lighthouse nebula (exposure corrected and smoothed with a gaussian kernel of  $\sigma=1.5$  pixel). The color scale at the bottom of the plot is in units of photon/cm<sup>2</sup>/s. Solid red rectangles “a”–“d” (and the corresponding dashed background boxes) were used to extract brightness profiles perpendicularly to the main jet (Sect. 2.3). The regions used for spectral extraction are also shown: solid black regions are used for the extraction of the mean spectra of the main jet, the counter-jet and the PWN (Sect. 2.4.1). For the point source PSR J1101-6101 we used a circle of radius 1.6'' centered on the pulsar position (not displayed). Background regions are marked with dashed black circles. In the inset: the details of the PWN shape and the attaching points of the two jets to the pulsar are visible. Colored rectangular regions along the PWN were used to extract spatially resolved spectra (Sect. 2.4.2).

from the pulsar, and to the presence of diffuse emission around the PWN edge, it is, however, impossible to verify whether this arc structure exists only between the pulsar and the base of the counter-jet, or if it extends further away. The arcs can be followed up to  $\sim 12''$  and  $18''$  from the pulsar, in direction to the main jet and to the counter-jet, respectively.

To reveal the signal in low surface-brightness regions, we extracted an adaptively binned image of the Lighthouse nebula. In order to do this, we applied the Voronoi tessellation algorithm developed by Cappellari & Copin (2003), as implemented in Eckert et al. (2015). We used a target S/N of 3 for the algorithm, which allows us to visualize statistically significant brightness variations across the nebula. The resulting image is shown in Fig. 2. All the known structures of the Lighthouse nebula (pulsar, PWN, main jet and counter-jet) are highly significant, as well as the diffuse emission around the main jet. This diffuse emission appears organised in “stripes” almost parallel to the main jet and more prominent at its far end. Closer to the pulsar, the algorithm is not able to resolve the apparent parallel lines (Fig. 1), the emission appears as more diffuse. This broad region of emis-

sion encircling the main jet is analysed in more detail in Sect. 2.3 and 2.5.

## 2.2. Pulsar proper motion

The absolute astrometric accuracy of 0.6'' of *Chandra* permits to perform sensitive proper motion searches of bright point-like sources and in particular of isolated pulsars, by comparing the position measured in observations separated by several years (see e.g. Auchettl et al. 2015b; Van Etten et al. 2012; Motch et al. 2009). Moreover, the relative positional accuracy between different observations can be significantly improved with respect to the absolute accuracy by removing systematic uncertainties that affect in the same way the different observations (see the *Chandra* documentation at <http://cxc.harvard.edu/cal/ASPECT/celmon/>). Here, we used our previous 50 ks observation and the new 250 ks *Chandra* observation of IGR J11014-6103 to search for proper motion of the pulsar (details of each observation are listed in Table 1). In each observation the pulsar is almost on-axis, although the telescope was operated in different configurations. To study

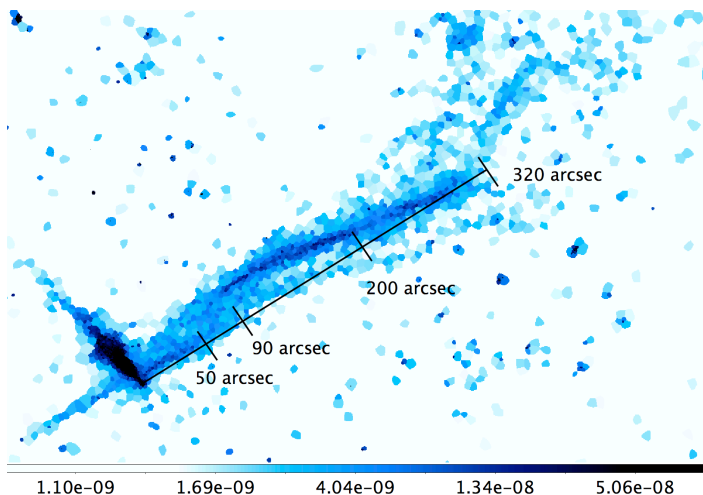


**Fig. 2.** Mosaic image of IGR J11014-6103 with Voronoi adaptive binning. Each cell in this image has a  $S/N \geq 3$ . The image is color coded in units of  $\text{photon}/\text{cm}^2/\text{s}/\text{arcmin}^2$  as detailed in the color map at the bottom of the plot. The pulsar, the main jet, the counter-jet, and the PWN are all detected at high significance. The broader emission around the main jet is also clearly detected. The black ruler shows linear distances along the jet.

the pulsar and the surrounding region, we used event files reprocessed without the *vfaint* mode background cleaning, as we included the old observation performed in *FAINT* mode. We used as reference frame obs.ID 16007, which has the longest exposure time (116 ks) and therefore the largest number of field point sources detected. We then registered all other exposures by creating a list of common field point sources with detection significance above  $4\sigma$  (within  $8'$  from the pulsar, to avoid including too strong boresite effects) between each frame and the reference one, to minimize the observed displacements. The CIAO tool *wcs\_match* was used to accomplish this. The number of common field sources between the reference frame (where we identified a total of 36 field sources satisfying the above criteria) and each other frame varied between 8 and 20, depending on the frame exposure. We corrected the reference positions for known proper motions of the field sources (we found 4 field point sources with optical counterpart in USNO B-2, for which a significant proper motion is known).

By comparing the residuals of the field source positions after registration of the frames, we found a relative positional accuracy of  $0.2''$  between all observations. We verified that inclusion or exclusion of the four sources with high proper motion does not affect the final positional accuracy. No significant pulsar displacement has been detected between the different epochs (which are approximately 2 years apart), resulting in a pulsar proper motion  $\mu_{\text{PSR}} \leq 0.3''/\text{yr}$  (at  $3\sigma$  level). This upperlimit is not constraining, it is consistent with the expected value of  $0.03''/\text{yr}$  ( $v_{\text{PSR}}/1000 \text{ km/s} \cdot (7 \text{ kpc}/d_{\text{PSR}})$ , assuming a pulsar velocity of 1000 km/s (Paper II).

### 2.3. Brightness Profiles

We extracted exposure-corrected, background-subtracted brightness profiles along the PWN and the main jet, using counts in rectangular regions. We defined 20 regions along the jet, extended for  $20''$  each, and 18 regions of  $5''$  length each along the PWN (see Fig. 3). From the counts recorded in each region we computed the brightness profiles with the CIAO tool

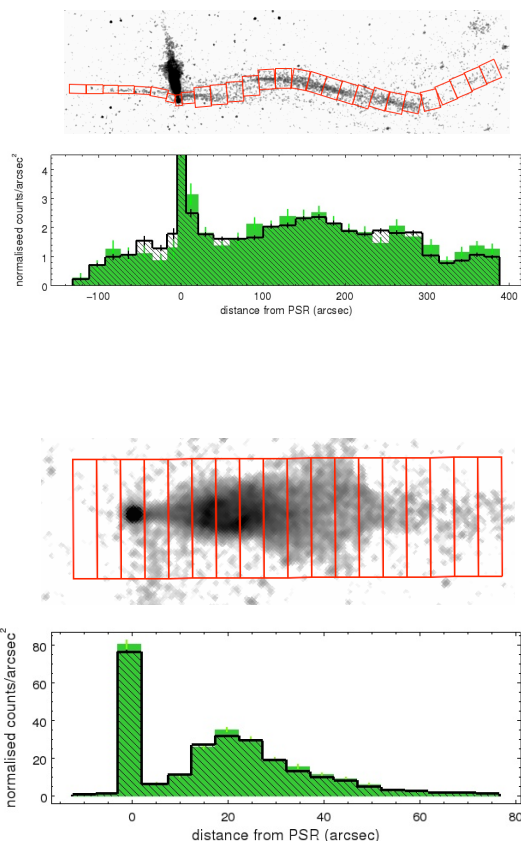


**Fig. 3.** Top panels: brightness profile as a function of distance from the pulsar, extracted along the jets (the brightness in the pulsar bin is not to scale), from the regions shown in the image above. The horizontal scale is the same in the profile plot and in the extraction region image. The black profile is extracted from the new 250 ks data, for comparison the profile obtained from the previous 50 ks observation is drawn as a filled green histogram. Bottom panels: same as above, but for extraction regions along the PWN.

*dmextract*. In Fig. 3 we compare the profiles extracted from the new 250 ks data with those obtained from the same regions in the old 50 ks observation. The images are normalised for the corresponding exposure maps, thus correcting for the effects related to the different integration time and satellite roll angle (and hence also the different positions of the chips gaps on the images). The brightness profiles do not show any relevant difference between the old and new observation (to within the uncertainties). At  $50$ – $90''$  from the pulsar, where the images seem to show a spatial break, we do actually not measure any significant brightness decrease with this choice of the profile extraction regions.

In our deep mosaic (Fig. 1), an additional diffused emission component is visible around the main jet. The Voronoi-binned image (Fig. 2) suggests that this emission comprises several “stripes” developing almost parallel to the main jet. To further investigate the structure of the region around the main jet, we computed the brightness profiles in different cuts perpendicular to the jet (Fig. 4). These profiles clearly highlight the presence of asymmetric X-ray emitting structures located both north and south of the main jet. Given the relatively low  $S/N$  of the data, we are currently unable to put firm constraints on the geometrical shape of these structures (but we speculate on possible modelling in Sect. 2.5).



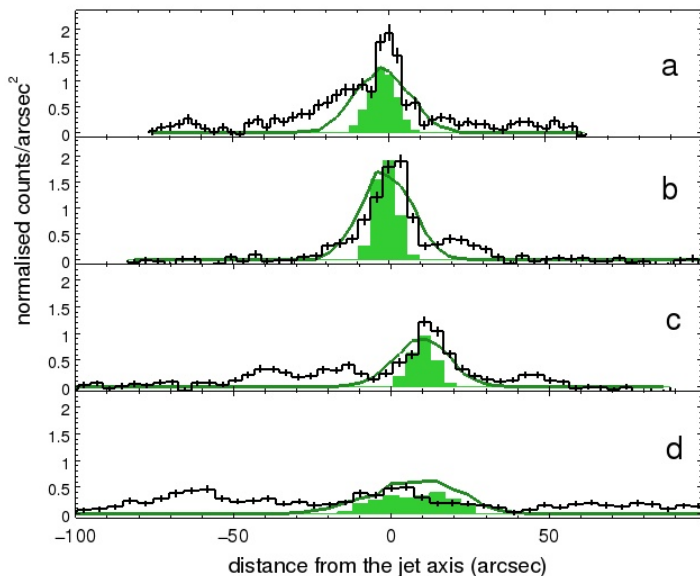


**Fig. 4.** Surface brightness profiles (black histograms) extracted in four cuts perpendicular to the main jet (see regions “a” – “d” in Fig. 1). We also plot for comparison the corresponding profiles obtained from a model with a single narrow (green histogram) or large (green solid curve) helical jet (see Sect. 2.5). In each plot the distance from the jet axis increases towards the pulsar direction of motion (SW).

## 2.4. Spectra

We extracted from each *Chandra* observation in Table 1 all the spectra that are described in Sect. 2.4.1 and 2.4.2, by using the CIAO tool *specextract*, computing at the same time the ancillary response file (ARF) and the response matrix file (RMF) of each dataset. We used the same extraction regions in all frames, and then combined the spectra of the same region with the CIAO tool *combine\_spectra*. This allowed us to obtain merged spectra with higher S/N and their corresponding weighted ARF and RMF. We verified that using the combined spectrum or fitting simultaneously the spectra from the various Obs-ID provides the same results within the statistical uncertainties. In the following we thus discuss only the merged spectra.

### 2.4.1. Average spectra of the extended regions

We extracted the average spectra of the pulsar, the PWN and the jets from the regions defined in Fig. 1. The extraction regions have been chosen to avoid the chips gaps in each exposure where possible (the only exception being the counter-jet and the PWN, which fall between two chips in all Obs-IDs).

All spectra are well described by a simple absorbed powerlaw model (reduced  $\chi^2 = 0.85$ – $0.99$ ). The results of the spectral analysis obtained from the fits to the pulsar, the PWN and the main jet are compatible with those reported previously in Paper II. Also the spectrum of the counter-jet is well fitted (reduced  $\chi^2 = 0.9$ ) with a simple absorbed powerlaw model. The best fit parameters are shown in Table 2. All spectra are interpreted as synchrotron emission from relativistic electrons, following the discussion in Paper II.

### 2.4.2. Spatially-resolved spectra

In order to analyse possible spectral variations as a function of distance from the pulsar, we extracted a number of spectra from small rectangular regions covering the PWN (as shown in Fig. 1). The regions follow the brighter part of the PWN, to maximise the S/N ratio. We used the same background regions as defined above. All these spectra could be well fit with a simple absorbed powerlaw model. The absorption column density remained constant within uncertainties. We then fixed the column density  $N_H$  among all regions of the PWN to the average value of  $9.9 \times 10^{21} \text{ cm}^{-2}$ . The photon index distribution is shown in Fig. 5. The photon index of the PWN X-ray emission increases noticeably with the distance from the pulsar. A fit with a parabolic function gives an acceptable description of the data (reduced  $\chi^2 = 0.7$ ) and provides a significant improvement with respect to the fit with a linear function (reduced  $\chi^2 = 2.6$ ).

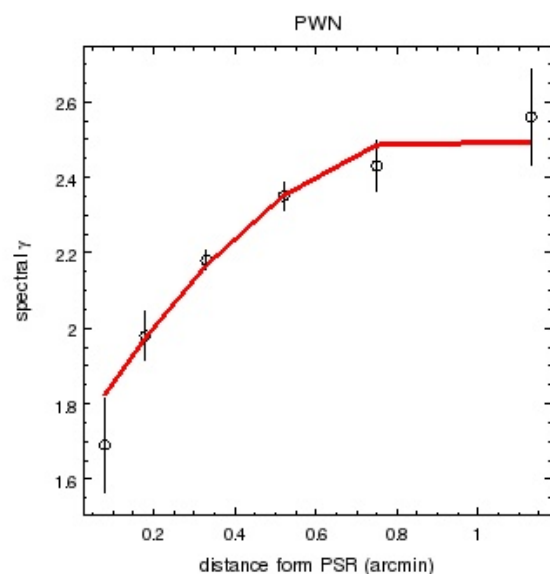


**Fig. 5.** Photon index along the PWN (uncertainties at  $1\sigma$  level). The best fit with a parabolic function is shown in red.

We performed a similar analysis of photon index along the main jet. In this case, however, a more complex variation of the photon index with the distance from the pulsar is found. To study these variations in more details, we extracted a photon index map (Fig. 6) using the method presented in Rossetti et al. (2007). We defined an adaptive 2D binning using the Voronoi tessellation technique presented in Sect. 2.1 with a target of 300 counts per bin. We then extracted the surface brightness in five logarithmically-spaced energy bands spanning the 1–6 keV range, where the main jet is predominantly emitting. We estimated the local background rate in each band and subtracted it from the data, adding in quadrature the uncertainty in the background rate. We then used XSPEC to fold the model spectrum with the *Chandra* response files to create a template of the expected count rate per band as a function of the photon index. The absorption column density was fixed to its mean value of  $N_H = 9 \times 10^{21} \text{ cm}^{-2}$ . A  $\chi^2$  minimisation procedure was then used to fit the templates to the spectra in each individual band and estimate the photon index with its uncertainty.

The photon index map confirms the smooth softening along the PWN, and the complex evolution of  $\Gamma$  within the main jet. To

**Table 2.** Best fit spectral parameters for the Lighthouse nebula components. All spectra were fit using an absorbed powerlaw model (photon index  $\Gamma$ ). Uncertainties are at 90% c.l. on the spectral parameters and 68% c.l. on the fluxes.

	$N_{\text{H}}$ ( $10^{22} \text{ cm}^{-2}$ )	$\Gamma$	$F_{2-10 \text{ keV}}$ ( $10^{-13} \text{ erg cm}^{-2} \text{ s}^{-1}$ )	$\chi^2/\text{d.o.f.}$
Pulsar	$0.88 \pm 0.09$	$1.08 \pm 0.08$	$6.2 \pm 0.15$	0.85 / 175
PWN	$0.99 \pm 0.05$	$2.22 \pm 0.06$	$6.1 \pm 0.1$	0.87 / 259
Main jet	$0.9 \pm 0.1$	$1.7 \pm 0.1$	$6.5 \pm 0.2$	0.99 / 233
counter-jet	$0.7^{+0.4}_{-0.5}$	$1.9^{+0.5}_{-0.6}$	$0.17^{+0.02}_{-0.04}$	0.9 / 12

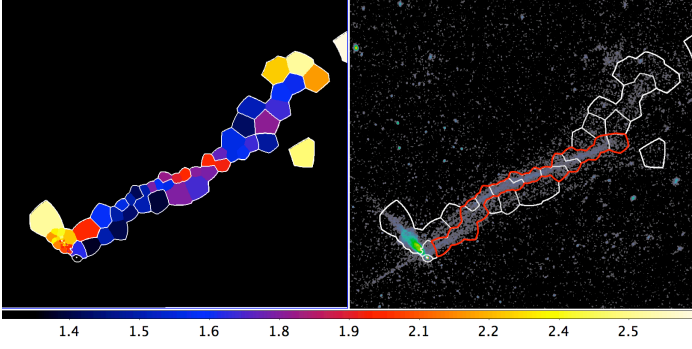


**Fig. 6.** Left panel: Photon index map along the main jet and PWN. The colors represent different spectral indices, as shown in the colorbar at the bottom of the plot. Contours are drawn around the regions for clarity, at levels of  $\Gamma = 1.1, 1.5, 1.8, 2.8$ . Typical uncertainties on the spectral indices are on the order of  $\pm 0.1$ . Right panel: the same contours are reported on the spatial map to aid the visual identification of the regions used for the spectral extractions, and of the regions clustering around similar values of  $\Gamma$ . The region in red was used to extract spectra from the main jet.

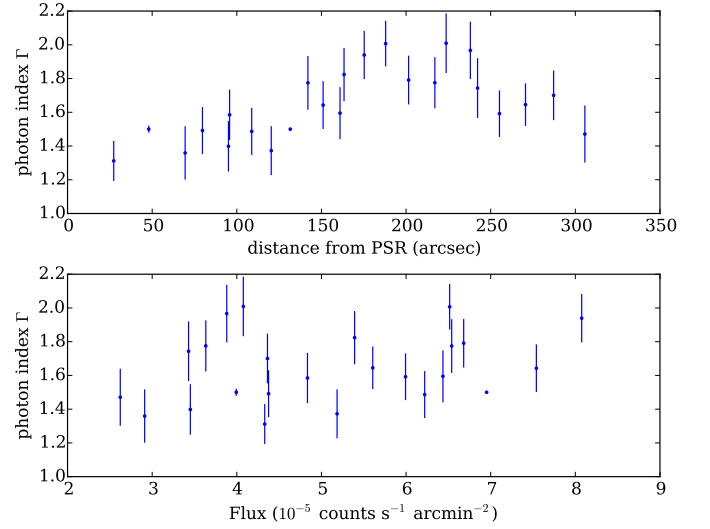


**Fig. 7.** Upper panel: photon index  $\Gamma$  as function of distance along the collimated main jet (see extraction region in red in Fig. 6). Bottom panel: as for the upper panel, but here plotted against flux in each Voronoi cell.

further characterise the spectral profile along the jet, we analysed first the correlation between  $\Gamma$  and the distance, and then between  $\Gamma$  and the flux. This analysis was repeated for the collimated main jet alone (red region in fig. 6), and for the brighter emission around it. In the latter case we did not find any significant correlation (the Spearman rank was  $R_{S_{\text{Dist}}} = 0.3 \pm 0.1$  and  $R_{S_{\text{Flux}}} = 0.4 \pm 0.1$ , respectively for the  $\Gamma$ -distance and for the  $\Gamma$ -flux relations). When considering only the collimated main jet, we found that  $\Gamma$  follows a curved trend as a function of distance (see Fig. 7). As the Spearman rank can not be used in the case of non-linear relationships, we split the sample into two groups: the linear correlation rank is  $R_{S_{\text{Dist}}} = 0.9 \pm 0.1$  up to  $200''$  from the pulsar, and  $R_{S_{\text{Dist}}} = -0.8 \pm 0.2$  between  $200''$  and  $320''$ , showing therefore a good correlation in the first portion of the main jet, and a slightly less significant anticorrelation in the farther part. Following the same separation up to  $200''$  and  $320''$  (again along the main jet only), we obtain for the  $\Gamma$  vs. flux correlation:  $R_{S_{\text{Flux}}} = 0.7 \pm 0.1$  up to  $200''$  from the pulsar, while no correlation is seen in the range  $200''$ - $320''$  from the pulsar ( $R_{S_{\text{Flux}}} = 0.1 \pm 0.3$ ).

## 2.5. Jet model

We applied the same 2D helical model described in Paper II to the new 250 ks image, to verify whether the helical pattern that we detected in the previous shorter *Chandra* observation can still fully account for this deeper observation. This is relevant in particular for the portion of the jet within the first  $100''$  from the

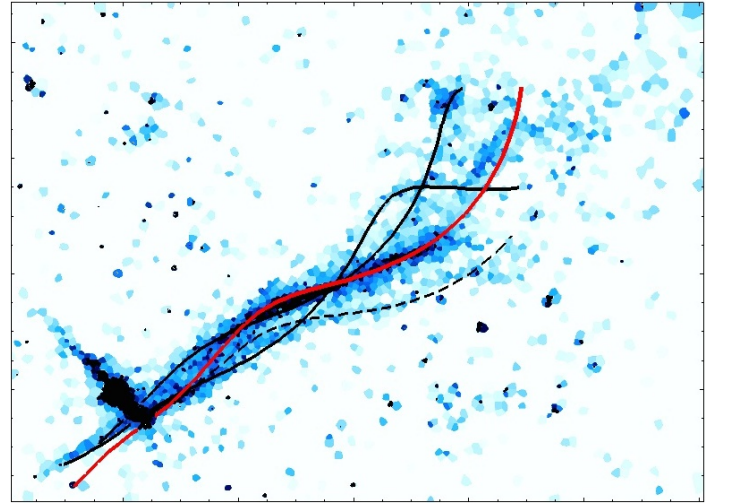


**Fig. 8.** Solid red line: best fit to the main jet with a simple helical model, superimposed to the 250 ks *Chandra* mosaic with Voronoi adaptive binning (Fig. 2). The model is in relatively good agreement with the shape of the jet at distances  $>200''$  from the pulsar, however it fails to reproduce the regions closer to the pulsar, and the counter-jet. In solid black lines are tentative additional helices, each with a different helical phase. A further tentative helix with different viewing angle is drawn with a dashed line.

pulsar, where the new data set confirmed the loss of a coherent line structure (see discussion in Sect. 2.3).

We used the *ciao*/*sherpa* tools and Python environment, and used the *cstat* implementation of the Cash statistic<sup>2</sup>. We fit the helical model to the mosaic image, using the corresponding exposure map, and adding a constant 2D function to simulate the background level. In our model we considered a fixed value for the particle bulk velocity  $\beta = 0.8$  (this value producing a good agreement for the observed ratio between the mean fluxes of the main jet and counter-jet, in the assumption that the two are intrinsically identical and the observed difference is only due to Doppler effects; Paper II). We restricted the modelling to the main jet, excluding counter-jet and the small scale arcs close to the pulsar.

The model includes a parameter used to modify the cross section of the helix around its axis (forming a 2D gaussian cross section). Given the presence of significant broad emission as discussed above (Sect. 2.1, 2.3, 2.4.2), we tuned this parameter a first time to match the brighter collimated main jet, and in a second case leaving the parameter free, to mimic the broader emission encompassing the main jet.

In all cases we found that the fit statistic significantly improved from a reduced value of 2.3 when only the background was included, to a value of 1.5 (for the helical model parameters: inclination angle  $38^\circ$ , helical period 60 yr, cone semi-aperture angle of  $4.5^\circ$ ; for the full description of the model parameters see Paper II). The residual map however shows that the image is not well reconstructed, with only the large scale features being reproduced. Limiting the fitting to the regions at distances greater than  $90''$  from the pulsar, to avoid the region of the spatial “gap” closer to the pulsar, does not provide a significant improvement in the fits results. The portion of the main jet closer to the pulsar fails to be fully reproduced by the same model parameters found for the farther part. If we include a helix symmetrical to the main one to model the counter-jet, this further strongly departs from the observed counter-jet direction (see the red line in Fig. 8). Comparison of the brightness profiles extracted from transversal cuts to the main jet (Fig. 4) shows that the single helix model does not follow sufficiently well the profiles measured from the data: the narrow helical model reproduces only in part the brightness peaks of the collimated main jet; and a broad helical model fails to reproduce the profiles observed from the extended emission around the jet.

Motivated by these mismatches of the single helix model, and by the presence of significant broad emission distributed non-symmetrically around the main jet (see transversal cuts in Figs. 2 and 4), we tentatively included additional helical outflows in the model (see Fig. 8). Given the relatively low surface brightness of this region, we did not attempt to fit this model to the data. We inspected only qualitatively whether this phenomenological model could improve the description of the broad emission encompassing the jet, with respect to the single helical model.

All the parameters describing the additional helices are fixed to match the ones used for the main helix, except for the helical phase and normalisation. Whereas we found that the main collimated jet was better described by an helix at phase<sup>3</sup> 260 deg, we found that the addition of further helices at phases 340 and 85 deg could mimic quite satisfactorily the extended emission

seen around the jet (without attempting a fit, we computed the corresponding statistic values with the *ciao* tool *calc\_stat* obtaining a reduced statistic of 1.4 for 15350 degrees of freedom). In addition a dim fourth helix with the same phase as the dominant one ( $260^\circ$ ) and slightly modified inclination angle of  $30^\circ$  could reproduce the emission observed south of the main jet at distances larger than  $200''$  from the pulsar (see Fig. 2). Together with the helical phase and normalisation, the three additional helices were also slightly shifted to match the main features of the broader emission. As a side result, the launching points of the additional helices come out to be aligned with the PWN axis, backwards with respect to the dominant helix.

### 3. VLT/FORS2 $H\alpha$ images

Our group obtained a VLT imaging observing run (run 092.D-0729, PI: Pavan), carried out in service mode with FORS2 (Appenzeller et al. 1998) at Cerro Paranal on December 23th, 2013. The aim of the observations was to search for a bow-shock created by the supersonic motion of the pulsar in the ISM.

The observations were performed using a narrow-band filter centered on the  $H\alpha$  line. The total exposure time in this filter was 1 hour 36 minutes. Additional short exposures ( $T_{exp}=35s$ ) were also taken with the R\_SPECIAL filter in order to have a handle on the continuum emission.

The images were reduced using the THELI pipeline (Schirmer 2013; Erben et al. 2005) which takes care of all processing steps, including bias subtraction, flat fielding, astrometric calibration and coaddition.

The  $H\alpha$  narrow-band images were calibrated by observing the spectrophotometric standard LTT4364 (Hamuy et al. 1992, 1994) with exposure times short enough to avoid saturation of the detector. These images were reduced in the same way as the science images. The tabulated flux of the standard star  $f(\lambda)$  was integrated within the filter transmission  $R_{H\alpha}(\lambda)$  and this value was compared with the measured count rate  $c_{H\alpha}$ . The derived zeropoint following this procedure is

$$k = \frac{\int f(\lambda)R_{H\alpha}(\lambda)}{c_{H\alpha}[\text{counts/s}]} = 3.97 \times 10^{-18} \text{ ergs s}^{-1} \text{ cm}^{-2} \text{ counts}^{-1} \quad (1)$$

Visual inspection of the narrow-band and continuum subtracted images (Fig. 9) reveals a general nebulosity over a large fraction of the field-of-view. This nebulosity together with the general crowding of stars, typical of the galactic plane, makes the detection of the bow-shock difficult. We computed upper limits on the bow-shock emission by placing 100 random apertures of  $1 \times 1''^2$  around the expected region of the bow shock, obtaining  $F(H\alpha)_{BS} \leq 1.25 \times 10^{-17} \text{ ergs s}^{-1} \text{ cm}^{-2} \text{ arcsec}^{-2}$  at the  $3\sigma$  level.

## 4. Discussion

### 4.1. Main jet

The new deep *Chandra* observation was optimised to avoid any instrumental feature falling along the main jet (chips gaps, dead columns). The mosaic image that we obtained (Fig. 1) confirmed the large scale spatial modulation of the main jet, as already detected in the previous *Chandra* observation (Paper II), as well as the presence of a spatial discontinuity along the main jet, between  $50''$  and  $90''$  from the pulsar. A significant broad emission surrounding the main jet is now also detected (see e.g. Fig. 2 and Fig. 4). Whereas in Paper II we found a good match between

<sup>2</sup> In *ciao*/*sherpa*, the *cstat* implementation provides an approximate goodness of fit, with the reduced statistic resulting of order 1 for good fits.

<sup>3</sup> the helical phase angle is computed from an arbitrary zero point



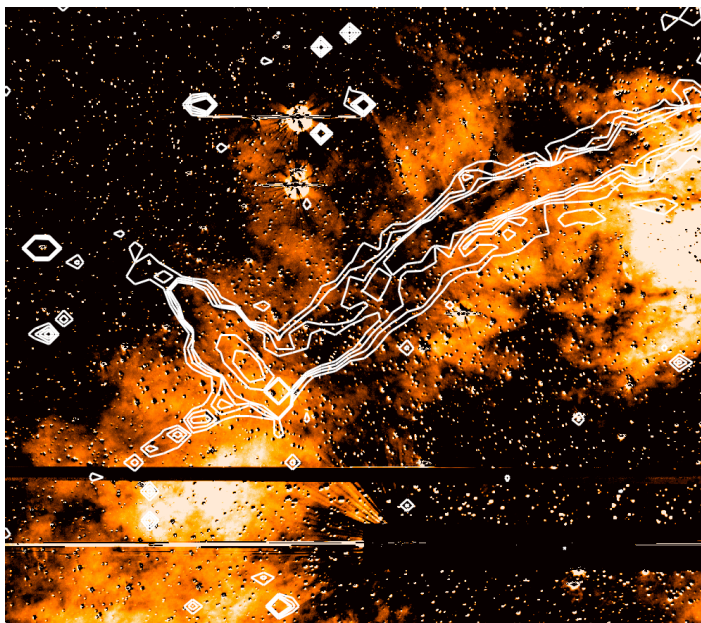


**Fig. 9.** The Lighthouse nebula region in H- $\alpha$  narrow band (continuum subtracted). Overplotted are the X-ray contours from the mosaic image in Fig. 1. At the bottom of PSR J1101-6101 a bright field star was masked with a MOS occulting bar. The diffuse emission is likely unrelated to the Lighthouse nebula, as discussed in the text, and prevents detection of any possible emission from a bow-shock in front of PSR J1101-6101.

the main jet and a simple helical model, in our new images the same model shows some discrepancies with the data. The helical modulation seem to be still a good first order approximation, but the higher statistics now available shows small scale departures from such a relatively simple picture. As discussed in Paper II, a helical pattern along a jet could be due either to a modulation of the jet launch direction by a free precession of the pulsar or to the development of kink instabilities along the jet (see e.g. Lyubarskii 1999; Moll 2010). In this latter case it seems natural to expect some small scale departures from an overall helicoidal trend. In particular, the spatial discontinuity of the main jet of IGR J11014-6103 might resemble the filament breaks described in laboratory plasma jets where macroscopic kink instabilities are accompanied by microscopic Rayleigh-Taylor instabilities occurring at particular regions along the magnetised plasma jet (Moser & Bellan 2012). These second instabilities can erode a portion of the plasma jet, either completely or partially, depending on the relative scales between the smallest filament diameter reached and the plasma ion skin depth level (Moser & Bellan 2012). Whereas the lab jets clearly develop on different scales with respect to the jet at hand here, the characteristics of jets produced in the laboratory are expected, as highlighted by the same authors, to be largely scale invariant and therefore applicable to astrophysical jets as well. The surface brightness profile extracted along the main jet of IGR J11014-6103 (Fig. 3) shows no significant decrease in the region of this spatial “gap”. The main jet in IGR J11014-6103 seems therefore to keep physically undisrupted. Under the kink instabilities scenario, the “gap” could then be interpreted as a region where the Rayleigh-Taylor instabilities would have failed to completely erode the jet. Alternatively, the gap region could be interpreted as the projected superposition of the main jet and the broader diffuse emission surrounding it, possibly due to several outflows (see below), degrading the coherence seen otherwise along other regions in the

jet. Conclusive evidences for intrinsic decollimation of the jet due to Rayleigh-Taylor instabilities or the superposition of several emission components to explain the diffuse emission along the gap cannot be derived from the observations reported here.

The photon index distribution along the broad region encompassing the main jet is rather complex, and no clear trend has been observed for the photon index neither as a function of distance from the pulsar, nor as a function of flux intensity (see Sect. 2.4.2). However, when restricting the analysis only to the brighter collimated main jet, we found a clear correlation between the photon index  $\Gamma$  and distance from the pulsar (see discussion in Sect. 2.4.2), with positive correlation up to  $200''$ , followed by anti-correlation between  $200''$  and  $320''$ . The first linear positive correlation between  $\Gamma$  and distance could be interpreted as softening of the emitting particles farther away from the pulsar, e.g., due to synchrotron losses. The sudden change to an anticorrelation at larger distances is however more difficult to explain in this scenario.

Keeping in mind the overall helicoidal modulation of the jet, we investigated the possibility that the variations in the observed photon index could be produced by the Doppler effect. When the synchrotron emission is produced by isotropically distributed electrons embedded in a magnetic field, the spectral index is a Lorentz invariant, i.e., if the intrinsic flux follows a power-law distribution in frequency space, the observed flux will also follow a power-law with the same index (see for example the discussions in Rybicki & Lightman 1979, see also Begelman et al. 1984 for extragalactic jets, and the treatment for different jet dynamics in Lind & Blandford 1985). If the spectrum is intrinsically curved, however, some further complexity may arise (see e.g., Fig. 5 in Fraix-Burnet 1997, for the case of a cutoff-power-law). For an approaching source, the Doppler boosting shifts the emitted frequencies towards higher observed frequencies in the observer frame. The observed spectrum could then appear overall harder than the emitted one, if the curvature in the emitted spectrum falls in a suitable range of energies.

In the case of a helical jet, as for IGR J11014-6103, assuming that approaching and receding regions intrinsically emit the same spectrum, one could then expect to observe harder spectra in approaching regions, if curvature or breaks are present in the original spectrum. Such breaks could be present in the data but possible be unresolved in the spectral fit. The total flux of the approaching regions would also be increased due to Doppler boosting, therefore one should expect an anticorrelation between photon index  $\Gamma$  and flux. Along the jet of IGR J11014-6103, however, the positive and negative  $\Gamma$ -distance correlation makes it difficult to explain the spectral modulation along the jet by Doppler boosting.

Alternatively, the complex photon index trend could arise from either particle re-acceleration along the jet (see, e.g. Rieger et al. 2007), or from varying conditions of the underlying magnetic field. In the latter case one would naively expect softening of the emission in correspondence to regions of higher magnetic field, where particles cool more efficiently. These same regions would yield also higher total fluxes, therefore providing a positive  $\Gamma$ -flux correlation. This could explain the spectral trend up to  $200$  arcsec, but not the hardening later on.

When applying the simple helical model discussed in Paper II to the jet-like features, we found that, while the single helical model can still reproduce the overall morphology of the jet, it fails to reproduce in particular the portion of the jet within the first  $100''$  from the pulsar and the counter-jet, both for the collimated main jet, and for the broader emission region around it (see Sect. 2.5). Whereas the counter-jet mismatch could be due



to non completely symmetric outflows and polar caps of the pulsar (as seen already both in isolated and in accreting pulsars, see e.g. Harding & Muslimov 2011; Bogdanov 2014; Venter et al. 2015), we noticed that the inclusion of several simultaneous helices with different launching phases could recover qualitatively the counter-jet direction. The different helices are naturally encompassing the main jet towards north or south directions depending on the distance from the pulsar, rather than being symmetric around the main jet. Although no fit of the multiple helices model was possible, due to the low surface brightness of the diffuse emission, the comparison between the region covered by the broad emission and the projection of the different helices hints towards an improvement of the modelling of this region with respect to a single broad helix. The complexity of photon index  $\Gamma$  with respect to both distance and flux could be at least partially relaxed in this case, as the broad emission would derive from the projection of several independent helices, each with a different projected  $\Gamma$  distribution. A side outcome of this model is that the launching point of the additional helices turns out to be aligned with the PWN axis and positioned backwards with respect to the dominant helix. This alignment may naively recall residual emission from the main jet, launched at different epochs in the past. However, in this ballistic jet model the past helices should be largely detached from the pulsar path, reflecting the travel time of the pulsar between the different launch points. The broad emission surrounding the main jet in IGR J11014-6103 is instead detected down to the launching points of the hypothetical additional helices. The tentative description of the broad emission encircling the main jet as being due to multiple helices necessarily needs therefore to involve the simultaneous presence of all of them.

A current hypothesis for the Crab jet foresees that the pulsar “jets” can be launched through the collimation of shocked wind plasma by hoop stresses in the wind magnetic field (Lyubarsky 2002). This would occur, in the Crab and other low velocity pulsars, in locations above the pulsar polar caps. Obviously, in this scheme no simultaneous presence of different helices is expected. In the case of a relativistic pulsar wind and strong velocity shears in the PWN we note, however, that the overall geometry and the occurrence of hoop stresses could be modified (see for example discussion in Kargaltsev et al. 2015).

An alternative interpretation for the main jet would be that of highly energetic particles being accelerated at the termination shock and then trapped by the underlying ISM magnetic field, as already proposed (and still debated) for the Guitar nebula (Bandiera 2008; Johnson & Wang 2010; Hui et al. 2012). The properties observed from the main jet only (photon index distribution, geometrical pattern, brightness profile) don’t provide however definite clues on either this model or the ballistic jet one. In the case of electrons diffusing into the ambient magnetic field, the existence of additional helices would require the presence of a very particular geometry of the ISM magnetic field. Also in this case, no trapping of particles by the ISM magnetic field is supposed to occur at places other than the front shock. At odds with the ballistic jet scenario, however, in the hypothesis of diffusion of particles in the surrounding magnetic field, past helices could show no significant detachment from the pulsar path, due to possible backwards diffusion of particles along the field lines. The “jets” would then be a visualisation of the ISM magnetic field in the surroundings of IGR J11014-6103 (compare for example the ISM magnetic field lines in Giacinti et al. 2013; see also the discussions on the Double Helix Nebula, Morris et al. 2006; Torii et al. 2014). The apparent organisation into helices that share the same parameters and differ only for the he-

lical phase angle would however pose severe difficulties to this scenario as well, in particular requiring these conical helices to have all the same aperture angle and to converge towards the pulsar location. To relax this apparent conflict, we note that the motion of the pulsar in the ISM could affect the distribution of the surrounding ISM material, together with its magnetic field.

#### 4.2. PWN

The magnetic field  $B_{\text{PWN}}$  in the PWN of the Lighthouse nebula was estimated in Paper II assuming that a single electron distribution was responsible for both the X-ray and radio emission observed along the tail. The angular separation between the emission peaks at these wavelengths, together with a flow velocity constrained to be  $v_{\text{flow}} \geq v_{\text{PSR}}$ , where  $v_{\text{PSR}} \gtrsim 1000$  km/s is the pulsar velocity through the ISM, was used to derive  $B_{\text{PWN}} \sim 10 - 20 \mu\text{G}$ . The new *Chandra* observations reveal a significant softening of the X-ray spectrum along the PWN axis. Close to the pulsar, the angular scales on which the variations are observed are as small as  $\sim 0.1' - 0.2'$ , which corresponds to a linear scale of  $\ell \sim 6 \times 10^{17} (d_{\text{PSR}}/7 \text{ kpc}) \text{ cm}$ . Assuming that the spectral variations are due to synchrotron losses of the electron population in the nebular magnetic field implies that the emitting population already cooled down while travelling these distances. Electrons mainly radiating in the  $\sim 1\text{-}10$  keV X-ray band require energies  $E_e \approx 45 (B_{\text{PWN}}/100 \mu\text{G})^{-1/2} (\epsilon/5 \text{ keV})^{1/2} \text{ TeV}$ , with  $\epsilon$  the X-ray photon energy. Equating the synchrotron cooling time for these X-ray emitting electrons  $t_{\text{sync}}(\epsilon) \approx 9 \times 10^8 (B_{\text{PWN}}/100 \mu\text{G})^{-3/2} (\epsilon/5 \text{ keV})^{-1/2} \text{ s}$  to the dynamic time for the cooling electrons to propagate within the nebula  $\tau \sim \ell/v_{\text{PSR}}$ , an updated value for the nebular magnetic field  $B_{\text{PWN}} \gtrsim 30 \mu\text{G}$  is retrieved.

The X-ray spectral profile along the nebula axis displays a monotonic steepening, ranging from  $\Gamma = 1.7$  to  $2.5$  (see Fig. 5), characteristic of synchrotron cooling. The softening rate is however higher at regions close to the pulsar, and flattens down at larger distances. Such profile differs from what is expected in a simple scenario in which radiating electrons are just advected away along the tail (see, e.g., the 1D toy model applied to the PWN N157B in Chen et al. 2006). Similar profiles for the X-ray photon index have also been observed in other PWNe, e.g. 3C 58 (Slane et al. 2004), G21.5–0.9 (Slane et al. 2000), or MSH 15–52 (An et al. 2014), and have been interpreted in terms of energy-dependent diffusion caused by Rayleigh-Taylor instabilities at the boundaries of the PWN and/or due to instabilities in the nebular magnetic field (Tang 2012; Begelman 1998). An unstable magnetic field structure deviating from a pure toroidal component may indeed be expected in the strongly perturbed nebula of IGR J11014-6103 given the high proper motion velocity of the system through the ISM.

The PWN initially opens up forming a wider cone, and includes also a more collimated tail visible up to  $60''$  from the pulsar (as described in Sect. 2.1). It could be compared to the structures seen in other bow-shock PWNe, and noticeably in the “Mushroom Nebula” powered by PSR B0355+54 (McGowan et al. 2006). The main differences between the two objects are the presence in the Lighthouse nebula of a strong narrowing region immediately behind the pulsar (up to  $7''$  from the pulsar, see Fig. 3), which is not seen in the Mushroom; and the absence of extended emission surrounding PSR J1101-6101. A displacement between the highest intensity of the bow-shock PWN and the pulsar location has been observed in the case e.g. of the Turtle nebula (PSR J0357+3205; De Luca et al. 2011, 2013; Marelli

et al. 2013). In this case, however, also an alternative interpretation was drawn, where the X-ray trail was modelled as thermal emission from the shocked ISM along the pulsar path (Marelli et al. 2013). In the case of PSR J0357+3205 no H- $\alpha$  emission was detected, since the surrounding ISM is fully ionised. Similarly, in the case of PSR J1101-6101, we could not detect H- $\alpha$  emission either (see Sect. 3), although the non-detection in our case is not conclusive given the presence of a large surrounding nebulosity. In the case of the Mushroom nebula, the presence of a jet has been invoked to explain the more extended “stem” part of the PWN. For IGR J11014-6103, the rotation axis may be oriented in the direction of the jet/counter-jet, so a new, roughly perpendicular outflow, which moreover falls right at the dissecting line of the PWN, seems difficult to justify. The presence of two different components in the PWN of IGR J11014-6103 could also be explained by differences in the magnetic field confinement, and by the presence of a strongly relativistic component of the wind (Bucciantini et al. 2005).

Besides the clear differences discussed above, we note that the X-ray emitting PWN population is characterised by a large variety of morphologies (see e.g. Kargaltsev & Pavlov 2008; Kargaltsev et al. 2015) and both the Mushroom nebula and the Lighthouse nebula could be explained under the same general bow-shock PWN model, assuming differences in the ISM and pulsar properties (for example alignment between the pulsar magnetic field axis and its direction of motion, or spin axis).

#### 4.3. Arcs

Much closer to the pulsar, towards the counter-jet, we observe in the *Chandra* mosaic a well defined arc structure (Fig. 1). The image also suggests the presence of a symmetric arc departing from the pulsar towards the main jet. It is not clear whether these structures directly connect smoothly to the jets, or whether they continue in the direction of the PWN (see Sect. 2.1). The “arcs” could be interpreted either as emission from the shocked ISM (a velocity of 1000 km/s, as the ones inferred for PSR J1101-6101, is indeed considered a lower limit for a shock to start emitting X-rays) or as outflows from the pulsar itself, in analogy to what is observed already in several other PWNs (see e.g. in Geminga, Kargaltsev et al. 2015).

#### 4.4. PSR-SNR association

Current 3D simulations drawn in the ideal case of non-rotating progenitor stars, predict that asymmetric ejections caused by hydrodynamic instabilities could impart strong kicks to a new born neutron star during a core collapse event (Janka 2012; Wongwathanarat et al. 2013). In this case, following Wongwathanarat et al. (2013), heavy elements should be distributed asymmetrically in the SNR, clustering in the direction opposite to that of the pulsar kick. To this aim we inspected the published results about a spatially resolved spectral analysis of SNR MSH 11-61A performed with XMM by García et al. (2012) and with Suzaku by Kamitsukasa et al. (2015). While the relatively large uncertainties obtained by Kamitsukasa et al. (2015) did not permit to detect differences in the abundances of the elements in these regions, the spectra and best fit results presented by García et al. (2012) clearly show (at a 7-10  $\sigma$  level) that the presence of the Fe line is much stronger in the NE and SW regions ( $\text{Fe}/[\text{Fe}_\odot] = 0.09 \pm 0.01$  and  $0.12 \pm 0.01$ , respectively) compared to the other regions analysed ( $\text{Fe}/[\text{Fe}_\odot] = 0.02 \pm 0.01$ ; the regions used by García et al. (2012) are reported also in Fig. 10), although no strong

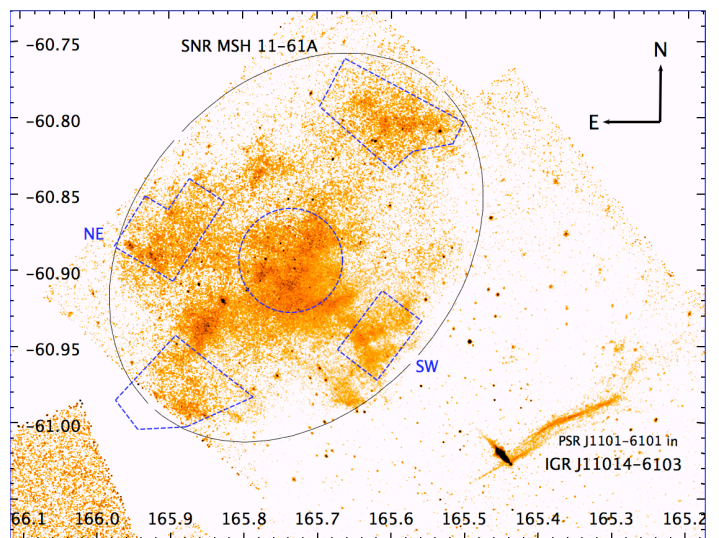


**Fig. 10.** Mosaic including all archival *Chandra* observations of the SNR MSH 11-61A and IGR J11014-6103 region. Dashed blue polygons are reproduction of the extraction regions used by García et al. (2012) for spectral analysis in the SNR (see discussion in Sect. 4).

variation between the direction towards (SW) and against (NE) the initial kick could be seen.

## 5. Conclusions

The overall structures of the PWN and main/counter-jet are confirmed in the new deep *Chandra* observations. The PWN appears now more clearly characterised by a bimodal shape, with a wide flow up to  $0.7'$  from the pulsar and a more collimated region extended up to  $1.7'$ . We observed a clear softening of the spectrum along the PWN, and retrieve a nebular magnetic field of  $B_{\text{PWN}} \gtrsim 30 \mu\text{G}$ .

The main jet still presents overall the same helical pattern seen in the previous observation, although several features at small and large scales cannot be fully explained in this model. A significant broad emission is detected around it, distributed asymmetrically with respect to the main jet axis. Different tentative interpretations of this outflow have been drawn in Sect. 4, in particular in the frame of a ballistic jet, possibly with kink instabilities, and in the frame of diffusion of particles in the local ISM magnetic field. None of them however can reproduce satisfactorily all observed spatial and spectral characteristics of the main jet, and the full interpretation of this feature remains open. A further hint for the presence of multiple flows is even more puzzling.

The lack of H- $\alpha$  detection (given the presence of strong surrounding nebulosity) and of detectable proper motion of the pulsar (given the relatively short timescale over which we could observe the pulsar, and its large distance to us) are both still fully compatible with the high linear speed assumed for this pulsar.

In Sect. 4 we also showed that the spectral properties of MSH 11-61A, derived by García et al. (2012), seem to agree with the general expectation drawn from the 3D simulations by Wongwathanarat et al. (2013), and with the prevailing picture of IGR J11014-6103 being formed during the same explosion that produced SNR MSH 11-61A.

**Acknowledgements.** The data analysed in this paper are based on *Chandra* and VLT observations obtained by our group. This research has made use of software provided by the *Chandra* X-ray Center (CXC) in the application packages CIAO, ChIPS, and Sherpa; the Heasarc tools provided by NASA <http://heasarc>.

gsfc.nasa.gov/ftools/ Blackburn (1995); and the ATNF Pulsar Catalogue (Manchester et al. 2005). We thank M. Capasso, S. Fotopoulou and C. Baldwin-Saavedra for useful discussions.

## References

- An, H., Madsen, K. K., Reynolds, S. P., et al. 2014, *ApJ*, 793, 90
- Appenzeller, I., Fricke, K., Fürtig, W., et al. 1998, *The Messenger*, 94, 1
- Auchettl, K., Slane, P., Castro, D., Foster, A. R., & Smith, R. K. 2015a, *ApJ*, 810, 43
- Auchettl, K., Slane, P., Romani, R. W., et al. 2015b, *ApJ*, 802, 68
- Bandiera, R. 2008, *A&A*, 490, L3
- Begelman, M. 1998, *ApJ*, 493, 291
- Begelman, M. C., Blandford, R. D., & Rees, M. J. 1984, *Reviews of Modern Physics*, 56, 255
- Blackburn, J. K. 1995, in *ASP Conf. Ser.*, Vol. 77, (San Francisco: ASP), ed. R. A. Shaw, H. E. Payne, & J. J. E. Hayes, 367
- Bogdanov, S. 2014, *ApJ*, 790, 94
- Bucciantini, N., Amato, E., & Del Zanna, L. 2005, *A&A*, 434, 189
- Cappellari, M. & Copin, Y. 2003, *MNRAS*, 342, 345
- Chatterjee, S. & Cordes, J. M. 2002, *ApJ*, 575, 407
- Chatterjee, S., Vlemmings, W. H. T., Briske, W. F., et al. 2005, *ApJ*, 630, L61
- Chen, Y., Wang, Q. D., Gotthelf, E. V., et al. 2006, *ApJ*, 651, 237
- Cordes, J. M., Romani, R. W., & Lundgren, S. C. 1993, *Nature*, 362, 133
- De Luca, A., Marelli, M., Mignani, R., et al. 2011, *ApJ*, 733, 104
- De Luca, A., Mignani, R. P., Marelli, M., et al. 2013, *ApJ*, 765, 19
- Eckert, D., Roncarelli, M., & Etori, S. e. a. 2015, *MNRAS*, 447, 2198
- Erben, T., Schirmer, M., Dietrich, J. P., et al. 2005, *Astronomische Nachrichten*, 326, 432
- Filipović, M., Payne, J., & Jones, P. 2005, *Serbian Astronomical Journal*, 170, 47
- Fraix-Burnet, D. 1997, *MNRAS*, 284, 911
- Gaensler, B. 2005, *AdSpR*, 35, 1116
- Gaensler, B., Swaluw, E., Camilo, F., et al. 2004, *ApJ*, 616, 383
- García, F., Combi, J. A., Albacete-Colombo, J. F., et al. 2012, *A&A*, 546, 91
- Giacinti, G., Kachelrieß, M., & Semikoz, D. V. 2013, *Phys. Rev. D*, 88, 023010
- Halpern, J. P., Tomsick, J. A., Gotthelf, E. V., et al. 2014, *ApJ*, 795L, 27
- Hamuy, M., Suntzeff, N. B., Heathcote, S. R., et al. 1994, *PASP*, 106, 566
- Hamuy, M., Walker, A. R., Suntzeff, N. B., et al. 1992, *PASP*, 104, 533
- Harding, A. K. & Muslimov, A. G. 2011, *ApJ*, 743, 181
- Hobbs, G., Lorimer, D. R., Lyne, A. G., & Kramer, M. 2005, *MNRAS*, 360, 974
- Hui, C. Y., Huang, R. H. H., Trepl, L., et al. 2012, *ApJ*, 747, 74
- Janka, H.-T. 2012, *ARNPS*, 62, 407
- Johnson, S. P. & Wang, Q. D. 2010, *MNRAS*, 408, 1216
- Kamitsukasa, F., Koyama, K., Uchida, H., et al. 2015, *PASJ*, 67, 16
- Kargaltsev, O., Cerutti, B., Lyubarsky, Y., & Striani, E. 2015, *Sp.Sc.Rev.[arXiv:1507.03662]*
- Kargaltsev, O. & Pavlov, G. G. 2008, *AIPC*, 983, 171
- Lind, K. R. & Blandford, R. D. 1985, *ApJ*, 295, 358
- Lyubarskii, Y. E. 1999, *MNRAS*, 308, 1006
- Lyubarsky, Y. E. 2002, *MNRAS*, 329, 34
- Manchester, R. N., Hobbs, G., Teoh, A., & Hobbs, M. 2005, *AJ*, 129, 1993
- Marelli, M., De Luca, A., Salvetti, D., et al. 2013, *ApJ*, 765, 36
- McGowan, K. E., Vestrand, W. T., Kennea, J. A., et al. 2006, *ApJ*, 647, 1300
- Moll, R. 2010, PhD thesis, Faculteit der Natuurwetenschappen, Wiskunde en Informatica
- Morris, M., Uchida, K., & Do, T. 2006, *Nature*, 440, 308
- Moser, A. L. & Bellan, P. M. 2012, *Nature*, 482, 379
- Motch, C., Pires, A. M., Haberl, F., Schwope, A., & Zavlin, V. E. 2009, *A&A*, 497, 423
- Pavan, L., Bordas, P., Pühlhofer, G., et al. 2014, *A&A*, 562, A122 (Paper II)
- Pavan, L., Bozzo, E., Pühlhofer, G., et al. 2011, *A&A*, 533A, 74 (Paper I)
- Reynoso, E. M., Johnston, S., Green, A. J., & Koribalski, B. S. 2006, *MNRAS*, 369, 416
- Rieger, F. M., Bosch-Ramon, V., & Duffy, P. 2007, *Ap&SS*, 309, 119
- Rossetti, M., Ghizzardi, S., Molendi, S., & Finoguenov, A. 2007, *A&A*, 463, 839
- Rybicki, G. B. & Lightman, A. P. 1979, *Radiative processes in astrophysics*
- Schirmer, M. 2013, *ApJS*, 209, 21
- Slane, P., Chen, Y., Schulz, N. S., et al. 2000, *ApJL*, 533, L29
- Slane, P., Helfand, D. J., van der Swaluw, E., & Murray, S. S. 2004, *ApJ*, 616, 403
- Tang, X. & Chevalier, R. 2012, *ApJ*, 752, 83
- Tomsick, J. A., Bodaghee, A., Rodriguez, J., et al. 2012, *ApJ*, 750L, 39
- Torii, K., Enokiya, R., Morris, M. R., et al. 2014, *ApJS*, 213, 8
- Van Etten, A., Romani, R. W., & Ng, C.-Y. 2012, *ApJ*, 755, 151
- Venter, C., Kopp, A., Harding, A. K., Gonthier, P. L., & Büsching, I. 2015, *ApJ*, 807, 130
- Wongwathanarat, A., Janka, H.-T., & Müller, E. 2013, *A&A*, 552, A126